


Diffraction effects and inelastic electron transport in angle-resolved microscopic imaging applications

A. WINKELMANN* , G. NOLZE†, S. VESPUCCI‡, G. NARESH-KUMAR‡, C. TRAGER-COWAN‡, A. VILALTA-CLEMENTE§, A. J. WILKINSON§ & M. VOS||

*Bruker Nano GmbH, Berlin, Germany

†BAM, Federal Institute for Materials Research and Testing, Berlin, Germany

‡Department of Physics, SUPA, University of Strathclyde, Glasgow, UK

§Department of Materials, University of Oxford, Oxford, UK

||Electronic Materials Engineering Department, Research School of Physics and Engineering, The Australian National University, Canberra, Australia

Key words. Electron backscatter diffraction, electron channelling patterns, electron diffraction, scanning electron microscopy.

Summary

O. C. Wells (1970) (Wells, 1970)

We analyse the signal formation process for scanning electron microscopic imaging applications on crystalline specimens. In accordance with previous investigations, we find nontrivial effects of incident beam diffraction on the backscattered electron distribution in energy and momentum. Specifically, incident beam diffraction causes angular changes of the backscattered electron distribution which we identify as the dominant mechanism underlying pseudocolour orientation imaging using multiple, angle-resolving detectors. Consequently, diffraction effects of the incident beam and their impact on the subsequent coherent and incoherent electron transport need to be taken into account for an in-depth theoretical modelling of the energy- and momentum distribution of electrons backscattered from crystalline sample regions. Our findings have implications for the level of theoretical detail that can be necessary for the interpretation of complex imaging modalities such as electron channelling contrast imaging (ECCI) of defects in crystals. If the solid angle of detection is limited to specific regions of the backscattered electron momentum distribution, the image contrast that is observed in ECCI and similar applications can be strongly affected by incident beam diffraction and topographic effects from the sample surface. As an application, we demonstrate characteristic changes in the resulting images if different properties of the backscattered electron distribution are used for the analysis of a GaN thin film sample containing dislocations.

Introduction

The image in the SEM can change completely if the position of the collector is changed.

Correspondence to: Aimo Winkelmann, Bruker Nano GmbH, Am Studio 2D, 12489 Berlin, Germany. Tel: +49 30 670990 8495; fax: +49 30 670990 30; e-mail: aimo.winkelmann@bruker.com

The scanning electron microscope (SEM) is a versatile tool for imaging purposes across a wide range of application fields. As the image formation process in the SEM is fundamentally governed by the local interaction of the incident electron beam with the sample, it is of central importance to have a comprehensive understanding of the complexity of the various signal generation mechanisms, which can be provided, for example *via* backscattered and secondary electrons, by Auger electrons, as well as by X-ray emission and cathodoluminescence (Venables *et al.*, 1986; Goldstein *et al.*, 2003).

In this respect, the detailed interaction physics of energetic electrons with condensed matter is of paramount importance, including the multiple elastic and inelastic scattering of the incident electrons. It is well known that angle-resolved detection of electrons in specific energy ranges can provide useful imaging modalities in the SEM (Niedrig, 1978; Wells, 1979; Reimer, 1998; Rau & Reimer, 2001). With the widespread availability of advanced two-dimensional (2D) imaging detectors in the SEM, an improved experimental characterization of the pertinent effects involved and their correct theoretical description by computational simulations acquires renewed importance (Wells *et al.*, 2012; Jaksch, 2012; Walker *et al.*, 2016; Forbes & Allen, 2016). This is the more so important in the case of crystalline materials, for which the signal generation process can obviously be influenced by diffraction effects due to the local crystal lattice, providing orientation contrast in the SEM (Prior *et al.*, 1996; Day & Queded, 1999; Wright & Nowell, 2006; Day, 2009; Schwarzer & Sukkau, 2013; Wright *et al.*, 2015).

As an example for advanced SEM imaging from polycrystalline materials, we show in Figure 1 a pseudocolour image of a deformed region found in an iron meteorite from Campo del Cielo (Buchwald, 1975). The image was obtained using an electron backscatter diffraction (EBSD) detector (e^- Flash^{HR+},

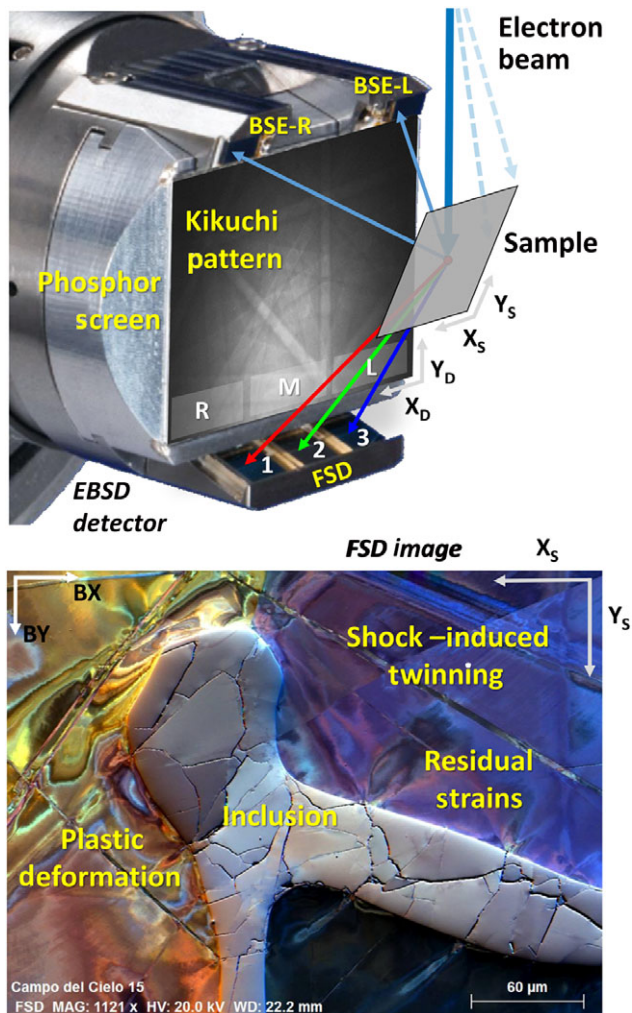


Fig. 1. Pseudocolour SEM image of the microstructure of an iron meteorite (Campo del Cielo) displaying strained regions due to plastic deformation around an inclusion of fractured schreibersite, and regions due to shock-deformation twinning (Neumann bands) which are visible as narrow stripes.

Bruker Nano, Berlin, Germany) equipped with a forward- and backscattered electron detection system (ARGUS™, Bruker Nano, Berlin, Germany). The pseudocolour image of the meteorite sample is derived from the electron signal collected by the three forward-scattering diodes (FSDs) as seen near the lower edge of the phosphor screen in Figure 1. The three FSDs 1, 2 and 3 in turn correspond to the red, green and blue colour channels. In the meteorite image, we can distinguish in the iron matrix an inclusion, which was subsequently determined *via* energy-dispersive X-ray spectroscopy and EBSD to consist of a phosphide (Schreibersite, $(\text{Fe,Ni})_3\text{P}$). This brittle inclusion is fractured by cracks presumably stemming from shock deformation of the meteorite. In the image, we also see shock-deformation twins (Neumann bands) as well as the results of significant plastic deformation with residual strains especially along the interface to the inclusion. All this crystallographical

information is available locally, with spatial resolution on the submicron scale, and a central purpose of this paper is to better understand the image formation process that leads to such rich information content from SEM images of polycrystalline materials. To study the signal formation process in the SEM under very controlled conditions, we conducted reference experiments at crystalline model systems. In these measurements, we are directly utilizing the EBSD pattern intensity captured on the phosphor screen of the EBSD detector shown in Figure 1. In this way, we are able to discriminate in a well-defined way between different angle-dependent effects that can possibly influence the signal generation process on angle-resolving detectors like the FSDs.

Predominantly, two closely related methods, EBSD (Dingley, 2004; Schwartz *et al.*, 2009) and electron channelling patterns (ECPs) (Joy *et al.*, 1982), are employed as diffraction methods in the SEM, with ECP also providing the foundation of electron channelling contrast imaging (ECCI) (Wilkinson & Hirsch, 1997; Zaefferer & Elhami, 2014). The main difference between these two methods is that, in ECP, diffraction effects are sensed predominantly *via* the incident beam, compared to diffraction effects in the outgoing directions for EBSD (Reimer, 1998; Wells, 1999). Both methods are based on the Kikuchi diffraction mechanism (Alam *et al.*, 1954), which conveys local crystallographic information on orientations and phases in the sample.

Our objective is to present and analyse measurements that clearly show that the interrelation of both types of diffraction effects, incident beam and outgoing beam diffraction, cannot be neglected for the diffraction-based imaging applications in the SEM once the angular acceptance in the incident and exit pathways is limited. The examples will demonstrate the implications of incident beam diffraction effects in nontrivial properties of the backscattered signal, most prominently in the angular dependence of the backscattered intensity distribution that is observed with angle-resolved, 2D detection typically applied in EBSD and in derived imaging modalities based on the angle-resolved detection of backscattered electrons (Payton & Nolze, 2013; Wright *et al.*, 2015).

Experimental and theoretical details

The main results of this paper in Section III.A.2 were measured on commercial Si(001). The measurements were carried out using a LEO 1530VP (Zeiss, Jena, Germany) field emission scanning electron microscope (FE-SEM) at an acceleration voltage of $E_0 = 20$ kV (beam current: $\approx <10$ nA). To optimize the effect of diffraction, the incident beam was maximally defocussed (working distance \equiv focus position: 50 mm) to better approximate an incident plane wave beam. By using low-magnification scanning ($45\times$), the angle of incidence is changing significantly with the spatial position of the incident beam, and thus an ECP can be observed on a single-crystal sample (Wells, 1974; Reimer, 1998). Moreover, this setup

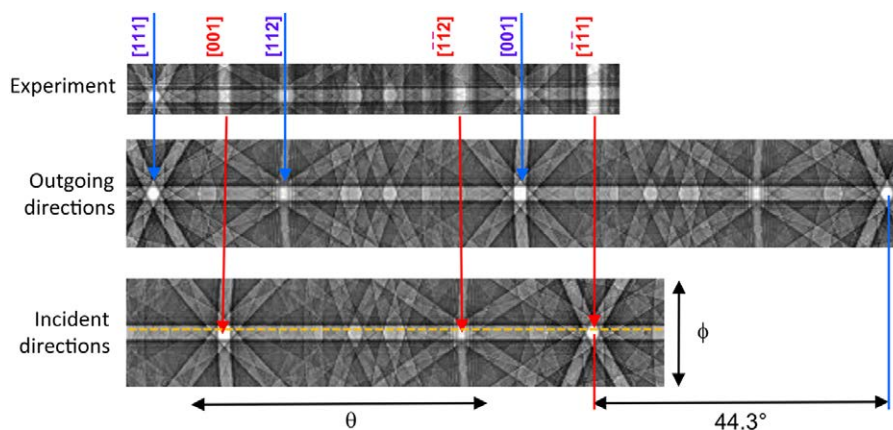


Fig. 2. Incident-beam channelling effects in silicon measured with an electrostatic electron energy analyser in a setup with fixed angle of 44.3° between incident and outgoing beam direction. In the experimental data, a vertically emphasized intensity for all outgoing directions ϕ occurs for incident directions near prominent zone axes. For an explanation of the geometry of the experiment and further details, see (Vos & Winkelmann, 2016).

simultaneously provides topographic reference contrast from, e.g. surface contamination, which allows us to compare the effects of diffraction and topographic changes on the outgoing intensity. For the ECP to be measured in a gnomonic projection even on a tilted sample surface, the tilt-correction of the SEM has to stay switched off.

Backscattered electrons (BSE) were collected by an EBSD detector using a standard measuring configuration with a 70° sample tilt as shown in Figure 1. EBSD patterns in 8bit mode with resolutions of 400×300 pixels have been stored for a total mapping grid of 640×480 measurement positions, which also represent an equal number of different incident-beam directions (acquisition time: 15 ms, detector-sample distance: 18 mm). The acquired raw EBSD pattern data were stored as measured, without further image processing, for the subsequent analysis (the data are available as a 37 GB file in HDF5 format). During the subsequent data analysis, we defined small rectangular regions of interest (ROI) in the stored raw EBSD patterns to extract angle-resolved intensity data for 'virtual FSD' (vFSD) imaging (see the vFSD-ROIs R,M,L in Fig. 1 in comparison to the real FSDs nearby).

To demonstrate the correct symmetry assignment to the outgoing and incident effects, we use a comparison of the measured intensity distribution patterns with simulated Kikuchi patterns (Winkelmann *et al.*, 2007) of Silicon as carried out using the software *ESPRIT DynamicS* (Bruker Nano). These simulations are also used to calibrate the gnomonic projection of the measured EBSD patterns for the position-dependent projection centre.

Results and discussion

Symmetry analysis

Combined effects of incident-beam and exit-beam diffraction. In order to shortly recall the basic understanding of the combined

role of the diffraction of incident and outgoing pathways in EBSD measurements (Reimer, 1998; Wells, 1999), we show in Figure 2 measurements that were taken under controlled conditions for incident and exit directions using a special electron spectrometer with a fixed geometry between the incident beam and the detected outgoing directions. For the details on the experimental setup and the measured data, see Vos & Winkelmann (Vos & Winkelmann, 2016).

The sample orientation relative to the incident and outgoing beam directions is controlled by rotating the sample around the θ -axis. The observed electrons have been scattered over a constant angle of 135.7° . In a backscattering geometry, this results in an exit direction that is 44.3° shifted in θ with respect to the incident beam, which is sampling approximately the horizontal dashed line in the lower panel of Figure 2. The exit directions are measured as azimuthal directions ϕ on the cone of constant scattering angles and are plotted along the vertical direction in Figure 2. Although the general pattern of the observed diffraction features in the experimental data corresponds to the symmetry of the exit directions (similar to EBSD), we also observe an increase in intensity when the incident beam is aligned with a strong zone axis as can be seen by the red arrows. In this case, the backscattered intensity is increased for all directions ϕ that correspond to a fixed incident beam direction, and this causes the vertical stripes in the experimental data. The data shown in Figure 2 clearly support the standard interpretation provided by the reciprocity principle (Reimer, 1998; Wells, 1999): When the incident beam is diffracted in such a way as to distribute electrons inside the crystal predominantly to the atomic sites, more electrons are backscattered (\rightarrow ECP). The modulated total number of backscattered electrons is then subsequently diffracted on the outgoing pathway (\rightarrow EBSD). The data shown in Figure 2 are fully consistent with this basic picture of the interplay between incident and outgoing beam diffraction. The following measurements will reveal an

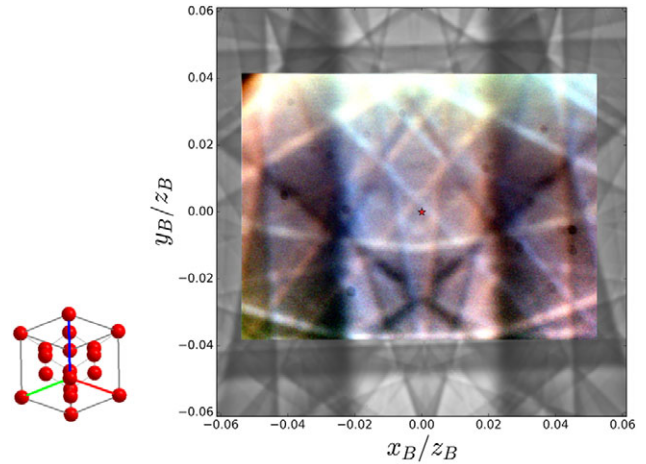
additional fine detail of this interplay, which will turn out to be absolutely crucial for SEM diffraction-based imaging applications.

Incident beam diffraction and the angular BSE distribution. The data in the previous section (Fig. 2) showed very clearly that the overall BSE intensity is affected by incident beam diffraction, i.e. there are in total more electrons backscattered and diffracted on the *outgoing* pathway when the *incident* beam electrons inside the crystal are redistributed into Bloch waves that overlap strongly with the atomic sites. This was proven by crystallographic correlation of the incident-beam direction with the observed BSE-intensity distribution. In addition to this straightforward total intensity effect, we will show in this section that there is also a concurrent change in the angular distribution of the varying total BSE yield. The combination of both, overall scaling and angular changes, can lead to nontrivial signal effects if electrons are collected in a limited range of scattering angles and energies only. This is why we will investigate in this section the impact of the incident-beam diffraction on the angular variation of the BSE signal, which will then lead us to the main result of this paper.

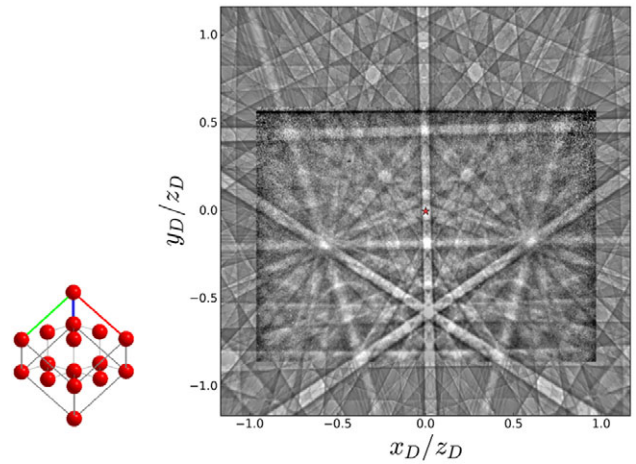
The measurements discussed in this section involve the scanning of an electron beam over the surface of an Si wafer and the simultaneous collection of electron backscatter diffraction patterns for each incident beam position (which is related to a corresponding incident beam direction). As can be seen by the ECP in Figure 3, the incident beam (A) covers a much smaller angular sector than does the outgoing signal seen in the EBSD pattern in (B). It is the characteristically different appearance of these two patterns that will allow us to recognize the effect of incident beam diffraction purely by the characteristic geometry and the symmetry of the ECP in Figure 3 (A).

For each of the 640×480 data points displayed in the ECP in Figure 3 (A), an EBSD pattern was collected and saved for further image processing. The applied image processing steps are shown in the left part of Figure 4. In Figure 4 (A), a representative raw EBSD pattern is given, (B) shows the smooth background (BG) obtained after low-pass fast Fourier transform (FFT) filtering and (C) displays the relative fraction of the raw EBSD pattern assigned to backscatter Kikuchi diffraction (BKD) as the difference of (A) and (B) normalized to the smooth background: $(C) = [(A) - (B)] / (B)$. Figure 4 (C) shows that the signal contribution that is due to the BKD features can reach about 10 to 15% relative to the background intensity.

To characterize the intensity distribution in the patterns in dependence on the beam position and thus also with respect to the incident beam diffraction, we need an image descriptor that can reliably capture the corresponding changes which are induced in the patterns. The centre of mass (COM) is among the simplest of a number of possible image descriptors (Jähne, 2005) that will react to changes in the relative image intensity distribution. We thus calculated the pixel position \mathbf{r}_{COM} of



(A) Incident beam diffraction: ECP



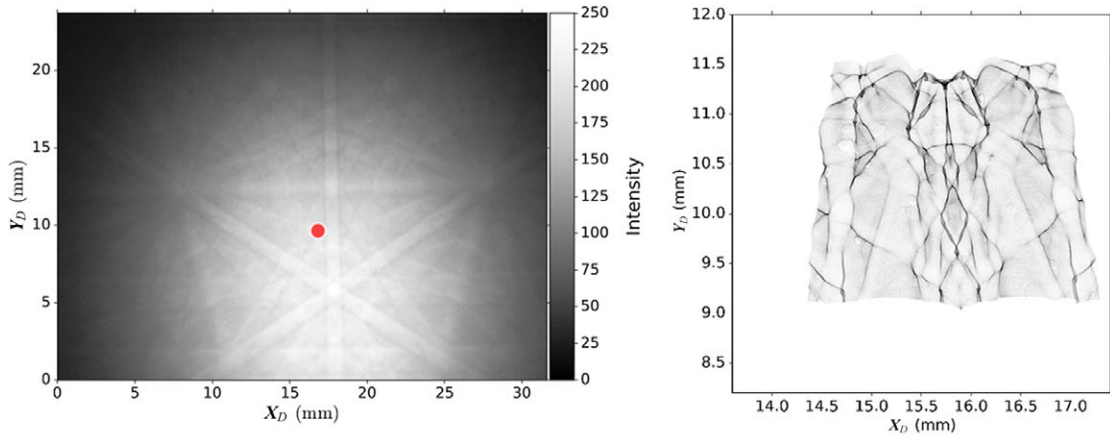
(B) Outgoing diffraction: EBSD

Fig. 3. Crystal geometry of incident versus outgoing directions. (A) ECP pattern due to low-magnification incident beam scan on a single-crystal Si(001) sample. (B) Representative EBSD pattern at one selected map position of the incident beam. The patterns are superimposed on corresponding simulations calibrated in gnomonic projection.

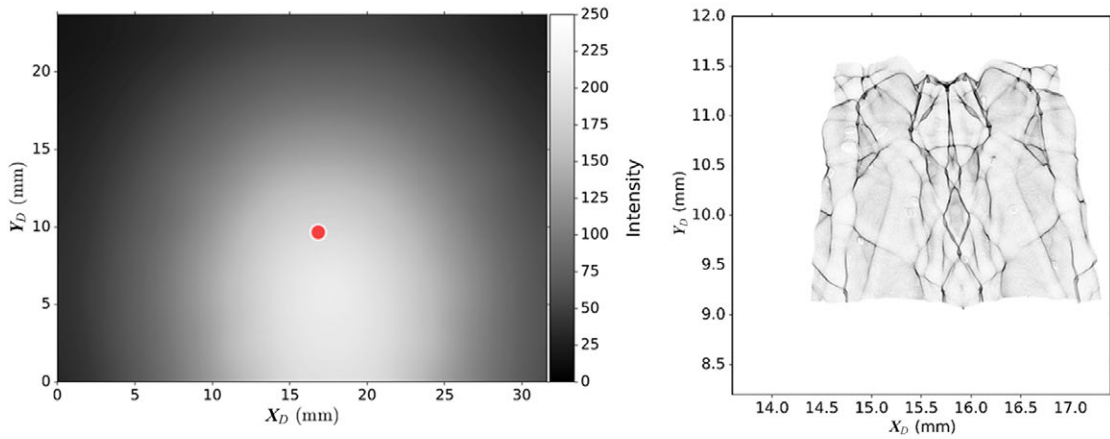
the COM of the measured images, with the pixel intensity interpreted as a mass density:

$$\mathbf{r}_{\text{COM}} = \frac{1}{\sum_P I(x_P, y_P)} \left(\frac{\sum_N x_N \cdot I(x_N, y_N)}{\sum_M y_M \cdot I(x_M, y_M)} \right) \quad (1)$$

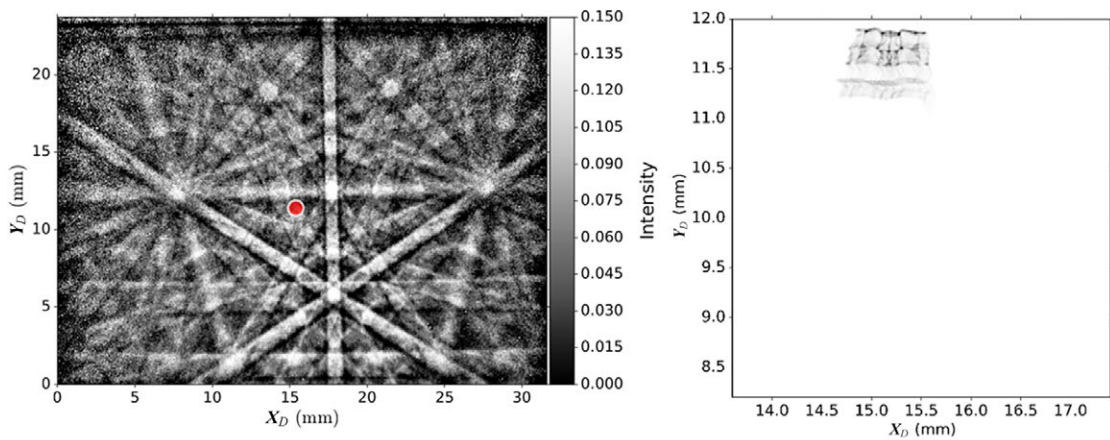
with $I(x_P, y_P)$ as the intensity at pixel P . Changes in \mathbf{r}_{COM} will serve as a proxy for changes in the angular distribution of the detected intensity, because a redistribution of intensity within the image will move the centre of mass. Moreover, for a Kikuchi pattern calibrated with respect to its gnomonic projection parameters, we can additionally assign to the 2D pixel \mathbf{r}_{COM} a corresponding three-dimensional unit vector that describes the direction from the projection centre (the beam spot on the sample) to the position of \mathbf{r}_{COM} on the detector



(A) Raw EBSD pattern



(B) Low-pass FFT filtered background (BG)



(c) Relative BKD fraction: $(\text{EBSD}-\text{BG})/\text{BG}$

Fig. 4. Data analysis of EBSD patterns: (A) raw pattern, (B) smooth background (BG) obtained by FFT filtering and (C) variation due to backscatter Kikuchi diffraction (BKD). On the right side, the distribution of the centre of mass r_{COM} is shown for the respective signal fraction of all 640×480 measured patterns.

screen. This will make it possible to quantify angle-dependent changes in the measured Kikuchi patterns.

The COM approach is model-free in the sense that it is largely insensitive to specific assumptions about, e.g. the actual shape of the background intensity and the signal-to-background ratio. The analytic form of these contributions is not exactly known in the general case, which limits the accuracy of optimization approaches that fit model parameters to the experimental data (e.g. assuming a 2D Gaussian function or a combination thereof to approximate the background).

The actual positions of \mathbf{r}_{COM} in the measured data are shown as examples by the red dots in Figure 4 for each specific EBSD signal contribution. In the right part of Figure 4, we plot \mathbf{r}_{COM} for all the 640×480 measured map positions which represent different incident beam directions. Using partially transparent discs for \mathbf{r}_{COM} , this allows us to visualize in a very direct way how \mathbf{r}_{COM} of the *outgoing* pattern changes with the beam position and thus with the angle of incidence of the *incident* beam. Each position of the COM is shown as a semitransparent disc. Overlap of discs is caused by deviations of the COM from a regular scanning grid and these deviations then produce the darker regions which are in accord with the symmetry of the incident beam geometry. The symmetric features in this distribution become immediately apparent to the eye.

The puzzling behaviour we observe in \mathbf{r}_{COM} is controlled by two main effects. First, \mathbf{r}_{COM} will change in a very regular way simply due to the regular scanning of the incident beam which can be seen to move the whole intensity distribution in the EBSD pattern on the phosphor screen right to left and bottom to top. This causes the overall roughly rectangular appearance of the area spanned by the \mathbf{r}_{COM} data points, with an approximate size slightly larger than 2×2 mm. This corresponds roughly to the area scanned by the incident beam (considering the clipping effects at the pattern borders). Imprinted on these regular changes caused by the systematically translated incident beam position, we can immediately recognize in Figure 4 (A) the strikingly symmetric deviations of \mathbf{r}_{COM} that lead to the appearance of a symmetric structure in the visualized data. The deviations resemble the crystal-lattice symmetry for the ECP seen in Figure 3. When looking at the patterns while the SEM beam is moving over the sample, we could thus possibly sense an additional shift of the intensity distribution when the beam is incident near the edge of an ECP Kikuchi band, where diffraction effects are strongest¹. In the absence of a relevant theoretical simulation, we cannot actually predict in which direction this additional shift in the background intensity will happen. However, all that is important for our general, symmetry-based argument is that we observe an effect with the symmetry of the incident beam geometry in the quantity \mathbf{r}_{COM} . Correspondingly, this means

that the effect on \mathbf{r}_{COM} must be influenced by diffraction of the incident beam. In accordance with Curie's Principle (Curie, 1894), the validity of this reasoning does not depend on the ability to quantitatively predict the effect in \mathbf{r}_{COM} ; it is purely the observation of a specific symmetry that allows us to conclude on the operation of a cause which has at most that symmetry (Shubnikov & Koptsik, 1974).

This interpretation can be further specified by the analysis of the BKD fraction of the EBSD pattern as shown in the bottom panel of Figure 4. The image processing removes nearly all of the background intensity and predominantly leaves the intensity variations due to the outgoing beam diffraction. As can be seen, this results in a substantial reduction of both the effects of the beam position change and the suppression of the incident beam diffraction features. The remaining changes in \mathbf{r}_{COM} of the BKD fraction are due to the changing gnomonic projection parameters, which translate the EBSD pattern in a regular way over the crystallographic features. This projective translation will still lead to a net change of \mathbf{r}_{COM} , which will be observed, however, at an overall different position that is determined by the structure of the BKD pattern, and not of the ECP. In striking contrast, in the middle panel of Figure 4, we observe for \mathbf{r}_{COM} basically the same behaviour as in the raw EBSD pattern if we take only the background part obtained by FFT-filtering. This contribution should be nearly devoid of any influence due to the exit path diffraction features seen in the lower panel. Compared to the smooth background intensity (B) as the dominating signal part, the outgoing diffraction effects of the BKD pattern (C) appear to be relatively insignificant.

The observations shown in Figure 4 thus lead to the main conclusion of this paper:

The smooth background intensity distribution in an EBSD pattern is influenced by diffraction of the incident beam in such a way that the centre of mass \mathbf{r}_{COM} of the EBSD pattern shows a change that corresponds to the symmetry of the incident beam geometry.

Such a symmetry-related change of the \mathbf{r}_{COM} -observable is due to a corresponding change in the angular distribution of the backscattered intensity distribution, which we illustrate schematically in Figure 5. The figure shows an idealized situation in an SEM at high magnification, characterized by a constant angle of the incident beam and the surface plane. We consider the formation of orientation contrast from grains in the sample. In this way, we exclude all effects on the BSE distribution which are not due to diffraction effects but which are caused by a changing angle of incidence to the surface as was discussed above. The total BSE yield near a Kikuchi band edge in dependence on the angle of incidence relative to a lattice plane is shown in Figure 5(A). As is well known, the Kikuchi band edge profile near a Bragg reflection is due to the selective excitation of two types of Bloch waves that distribute electrons predominantly onto atomic sites for angles slightly smaller than the Bragg angle, case (H), or between atomic sites for angles larger than the Bragg angle, case

¹ In the Supplementary Figure S1, we give a high-resolution plot of the data shown in Figure 4 (A), which should enable the reader to study the intricate and strikingly beautiful details of the experimental \mathbf{r}_{COM} distribution.

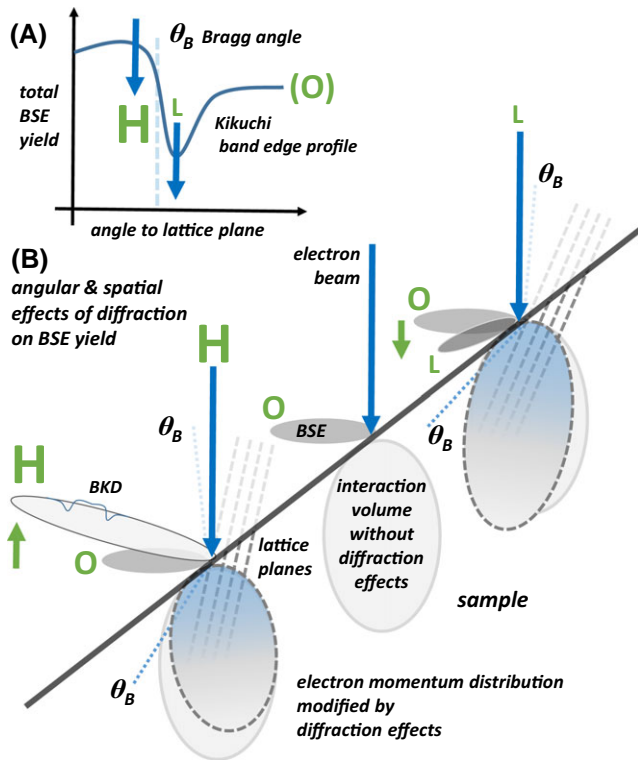


Fig. 5. Schematic representation of the influence of diffraction effects on the angular distribution of backscattered electrons. (A) Total BSE yield in dependence on the angle of incidence near a Kikuchi band edge. The edge profile is due to the selective excitation of Bloch waves near a Bragg reflection (Joy *et al.*, 1982). (B) The corresponding qualitative changes in the angle-resolved BSE distribution, relative to a reference situation (O) with negligible diffraction effects. The angular BSE distribution is changed in dependence on the relative orientation of the local surface plane, the incident beam and the reflecting lattice planes in the probed region of the sample. In accordance with panel (A), the total BSE yield is *increased* for an angle of incidence (H), but the angular BSE distribution is also *tilted* relative to (O). Similarly, the BSE yield is *reduced* and *tilted* differently for the angle of incidence (L). The changes of (H) and (L) relative to (O) are due to the influence of diffraction effects on the scattered electron momentum distribution inside the sample, which correspondingly modifies the electron distribution in direction and energy outside the sample. We note that the angular changes shown are purely qualitative and do not imply a prediction of the actual size and direction of the observed changes. Quasielastic backscattered Kikuchi diffraction (BKD) is a comparatively small effect relative to the modulation of the total, elastic and inelastic, BSE distribution.

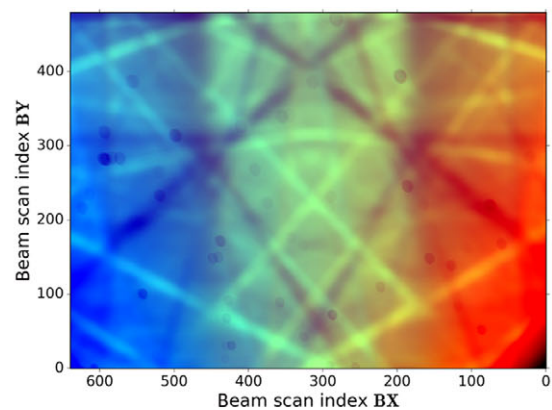
(L). This correspondingly leads to higher (H) or lower (L) total BSE yield (Joy *et al.*, 1982). The spatial and angle-dependent details of the backscattering process which was characterized only by the total yield in part (A) of Figure 5 are specified in Figure 5(B). This part of the figure additionally illustrates the corresponding qualitative changes in the angle-resolved BSE distribution when the total yield is changing. Relative to a reference situation (O) without diffraction effects, the angular

BSE distribution is changed in dependence on the relative orientation of the local surface plane, the incident beam and the reflecting lattice planes in the probed region of the sample. In accordance with panel (A), the total BSE yield is *increased* for the angle of incidence (H), but the angular BSE distribution is also *tilted* relative to (O). Similarly, the BSE yield is *reduced* and *tilted* differently for the angle of incidence (L). The changes of (H) and (L) relative to (O) are due to the influence of diffraction effects on the scattered electron momentum distribution inside the sample, which correspondingly modifies the electron distribution in direction and energy outside the sample. As shown by the previous Figure 4(C), the quasielastic BKD is a comparatively small effect (order of magnitude 10% or less) relative to the modulation of the total, elastic and inelastic, BSE distribution.

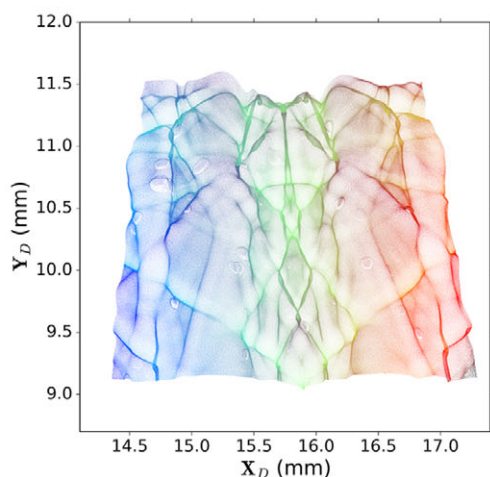
With the main message of this paper stated, the remaining part of this paper serves to discuss some of the implications that follow from the fundamental influence of incident beam diffraction that was disclosed by the results in Figure 4.

Despite the fact that the change in the angular distribution seems to be relatively minor, the effect revealed in Figure 4 is decisive for differential signal generation in imaging applications on crystalline materials. If solely an overall scaling effect of the total backscattered intensity is assumed to result from the incident beam diffraction (similar to what is shown in Fig. 2), a colour change in pseudocolour imaging cannot be easily explained, because this would scale all three colour channels by a common factor. In this case, only the net intensity would be changed but not the relative weights of different colour channels, which is necessary to change the resulting colour signal.

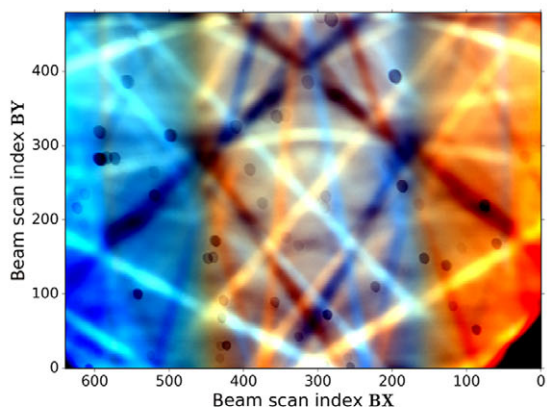
The correlation of the colour changes in pseudocolour virtual FSD imaging with the observed changes in r_{COM} is shown in Figure 6. In this figure, the colour signal that would be assigned to a beam position (BX, BY) in the multi-FSD SEM image (top panel) was also attached to the respective r_{COM} of the EBSD pattern measured at that beam position. By comparison of the colours in the upper and middle panel of Figure 6, the actual movement of r_{COM} can be directly traced. As seen from the detector phosphor screen, the SEM scan starts in the lower right, proceeding to the left along the negative X_D -axis and upwards along the positive Y_D -axis of the detector as defined in Figure 1 (for an analysis of the relevant geometries, see also (Britton *et al.*, 2016)). In terms of colours assigned to the signal from the ROIs R/M/L while scanning, the beam moves over the sample surface in a regular way: each SEM scan starts near the R ROI and ends nearer to the L area. Since this movement is continuous, this leads to a smooth red-green-blue change from left to right. This smooth colour change underlies the diffraction features in the pseudocolour BSE data. We note that the SEM image shown in Figure 6 has been rotated by 180° with respect to the image that would usually be seen on the SEM display (e.g. the ECP in Fig. 3) in order to conform to the symmetry of the beam movement in



(A) vFSD-RGB bottom



(B) Positions of the centre of mass in the EBSD patterns. The colour corresponds to the incident beam indices in (a)



(C) vFSD-RGB bottom, after correction for PC

Fig. 6. Assignment of the SEM beam scan index coordinate (BX, BY) to the corresponding positions r_{COM} of the the centre of mass. The colours are assigned based on the signals in the R/M/L regions of interest in the EBSD patterns (R = red, M = green, L = blue, compare Fig. 1). The image in the lower panel was calculated after reprojection of all EBSD patterns to a common projection centre and detected solid angle, thus removing a large part of the variations due to the translation of the beam position relative to the detector.

the detector coordinate system (Jackson *et al.*, 2014; Britton *et al.*, 2016).

For the single-crystal sample observed here, the incident beam diffraction variations in r_{COM} are not large enough to overcome the smooth changes which are caused by the movement of the beam from left to right (blue to red) and bottom to top (light to dark) of the sample, as can be seen in the top panel of Figure 6. Although the regular variation due to the beam spot translation on the sample surface can be accounted for by a correction procedure (see below), it is already obvious from the uncorrected data in Figure 4 that the changes in r_{COM} will be dominating in the limit of only small beam movements at high magnifications of polycrystals. In this case, the changing crystal orientations in the imaged area will provide differential incident beam diffraction as compared to the direct change of the angle of incidence as deployed in the model experiment here. Also, at high magnification, the specific influence of the surface plane inclination relative to the incident and the outgoing electrons is then relatively constant in the absence of any additional topographic changes.

To remove the effect of the beam movement on the sample, and thus a movement relative to the R/M/L ROIs, we corrected all the measured EBSD patterns for this effect by determining the projection centre from the EBSD patterns and gnomonically reprojecting each individual pattern to a solid angle that is common to all measured patterns. The projection centres were determined by a best-fit pattern matching procedure using dynamically simulated patterns assuming a fixed orientation of the Si crystal and only varying the PC coordinates. The result of the correction procedure is seen in the lower panel of Figure 6, where the colour changes are now much more pronounced when applying the same ROI-based analysis as for the upper panel. Specifically, we can see some differently coloured lines left and right from the middle. This can be interpreted as being due to a mirror-symmetric angular movement of a component in the BSE distribution when the respective mirror-symmetric incident beam diffraction conditions are met.

Returning to the implications of the changes observed in r_{COM} , the same underlying mechanism will also cause severe changes in calculated ECPs extracted from the measured EBSD patterns. The calculated ECPs derived from the angle-resolved EBSD pattern intensity on a vFSD ROI can be directly compared to conventional ECPs measured with electron detectors at different collection positions (Ichinokawa *et al.*, 1974; Wells, 1979). As is shown in Figure 7, a calculated ECP derived from the top part of the phosphor screen can show an inverted intensity contribution compared to the corresponding ECP from the lower part of the screen. This needs to be taken into account for the data interpretation in ECP-based diffraction methods like ECCI if the relevant electrons are detected from a restricted angular range only. If the signal for the ECP is collected from a restricted area, in principle there can be two opposite situations where the angular maximum of the BSE intensity is moving either into the fixed detection

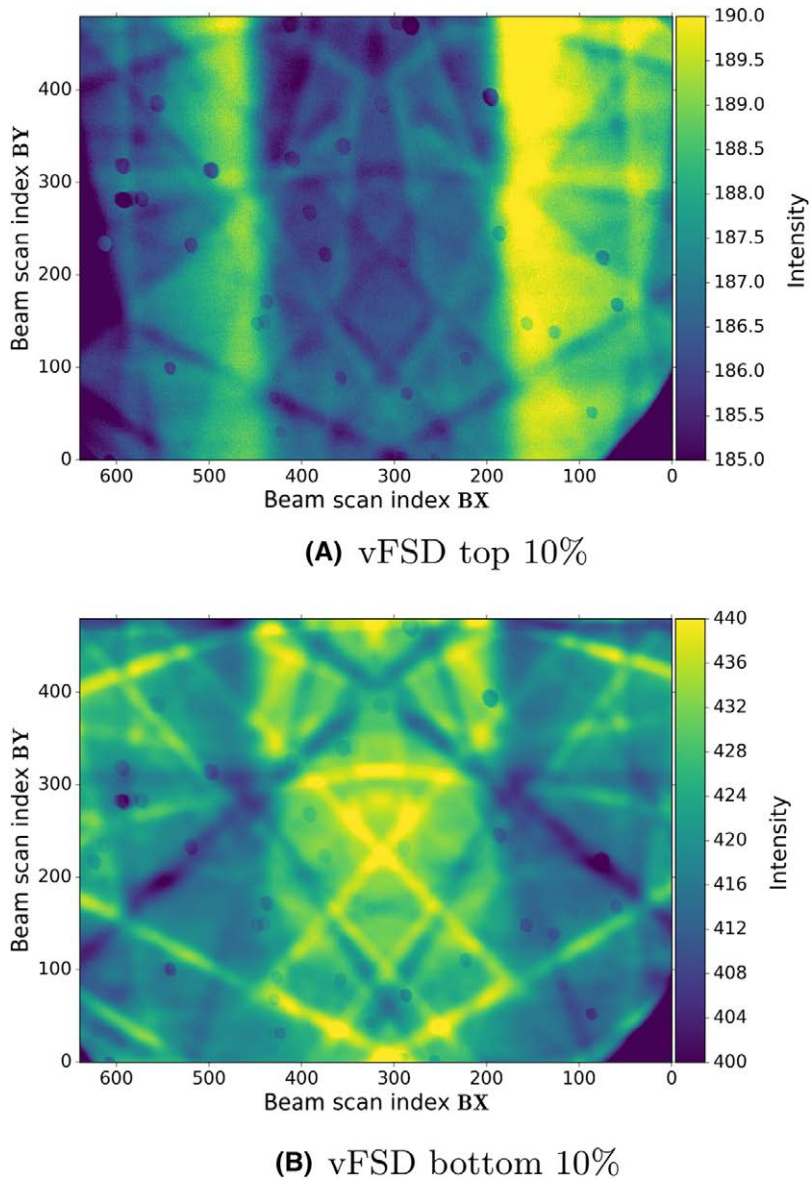


Fig. 7. Calculated ECPs derived from top versus bottom vFSD regions in the EBSD patterns.

area or it is moving out of the fixed detector area when a Bragg reflection of the incident beam occurs. This in turn will lead to opposite contrast changes when the incident beam traverses a predefined diffraction situation near a Bragg angle. In this way, the angular intensity changes in a restricted detector area can possibly counteract the intensity changes due to total yield variation. For an up-down change of the intensity maximum, it is obvious that opposite intensity changes could be observed with electron detectors placed on the top compared to the bottom part of a phosphor screen. These opposite contrast changes, however, would correspond to exactly the same orientation changes of the relevant crystal regions. Care must thus be taken when interpreting ECC images from

dislocations if the theory used for the image simulations does not include the detailed channelling-in effects on the outgoing electron distribution. If the simulation approach does not provide means for inclusion of the channelling-in effects on the energy- and momentum distribution of the backscattered electrons, suitable experimental conditions which are free of these effects should be used for ECCI. In particular, the effects of angular changes of the BSE intensity on ECCI will be minimized if the collected BSE signal is effectively proportional to the total integrated BSE yield. This is probably the case in the majority of ECCI investigations using conventional BSE detection optimized for highest yields. In this case, the basic interpretation of the modulation of the total backscattered intensity

by the incident beam diffraction (Joy *et al.*, 1982) will be still valid.

The results obtained so far can be put into perspective by a comparison to the existing literature. It is well known that strong contrast changes can be observed when changing the collector position even on noncrystalline samples (Wells, 1970). Thickness effects and the influence of the primary beam energy on the angular distribution of backscattered electrons have also been previously found (Hohn & Niedrig, 1972; Hohn, 1977; Niedrig, 1977, 1982; Böngeler *et al.*, 1993; Spranck *et al.*, 1995). In the context of investigations on crystalline samples, a rather complex behaviour of diffraction contrast in ECPs observed under angle-resolving conditions was demonstrated by various authors (Ichinokawa *et al.*, 1974; Yamamoto, 1977a, 1977b; , 1977c; Yamamoto *et al.*, 1978; Wells, 1979; Reimer *et al.*, 1986; Wilkinson & Hirsch, 1997).

Taking these previous findings into account, it is possible to rationalize the observed changes in the shape of the distribution of backscattered electrons. In a first step, diffraction *via* coherent elastic scattering of the incident beam in the crystal will lead to the excitation of Bloch waves composed of wave vectors pointing in different directions, which are related to the direction of diffracted beams that would be observed on the exit side of a thin sample. This means that the incident beam diffraction starts to redistribute electrons into directions which are modified with respect to an amorphous sample. This initial electron redistribution will likewise affect any subsequent inelastic scattering processes so that the overall electron transport is modified by the diffraction in the beginning and during the scattering cascade. Anomalous absorption effects can additionally contribute to a modified depth-distribution of the electrons scattered inside the crystal (Peng *et al.*, 2004). A pertinent treatment of the electron transport problem in the presence of diffraction has been given by Dudarev *et al.* in (Dudarev *et al.*, 1995; Peng *et al.*, 2004). As demonstrated in (Dudarev *et al.*, 1995), the approach used by Dudarev *et al.* successfully reproduced observations of contrast inversion effects which depend on the electron detector position (Ichinokawa *et al.*, 1974), and which are very similar to the results shown in Figure 7.

In the experiments we have discussed above, the effect of sample topography was deliberately minimized by using a polished commercial Si wafer. In the general case, however, topographic changes will also affect the angular distribution and thus \mathbf{r}_{COM} of the backscattered electrons (Reimer, 1998). On inspection of the \mathbf{r}_{COM} data in Figures 4 and 6, the impact of some topographic features (e.g. due to residual particles) on the sample can still be clearly seen. As the present experiment was carried out with a defocused beam, this increases the diffraction contrast and blurs topographic features. However, the strong influence of topographic features in the resulting pseudocolour data can be seen in the lower panel of Figure 6. This is why, topography is a major effect that needs to be taken into account when interpreting experimental SEM pseudocolour

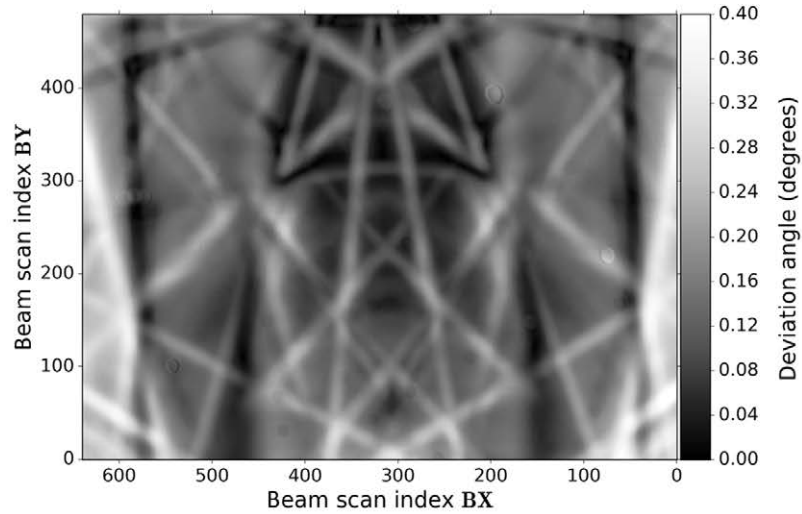
images. Seen from a different perspective, the diffraction effects can also limit the sensitivity of methods to determine the local surface topography *via* angle-resolved detection of the backscattered electron distribution (Hejna, 1995, 2008; Picard *et al.*, 2008; Zaefferer & Elhami, 2014; Wright *et al.*, 2015; Chapman *et al.*, 2016). If the local changes of the topographic surface plane inclination angle are in the order of the effects due to incident beam diffraction, it can be challenging to disentangle both effects in the angle-dependent BSE intensity observed.

As Monte-Carlo simulations of electron scattering are increasingly used for image interpretation and data analysis in the SEM (Joy, 1995; Werner, 2001; Dapor, 2014; Walker *et al.*, 2016), the interrelation between topographic and orientation contrast mechanisms is another example for the need to ultimately include in Monte-Carlo simulations the nontrivial consequences of diffraction effects as discussed above.

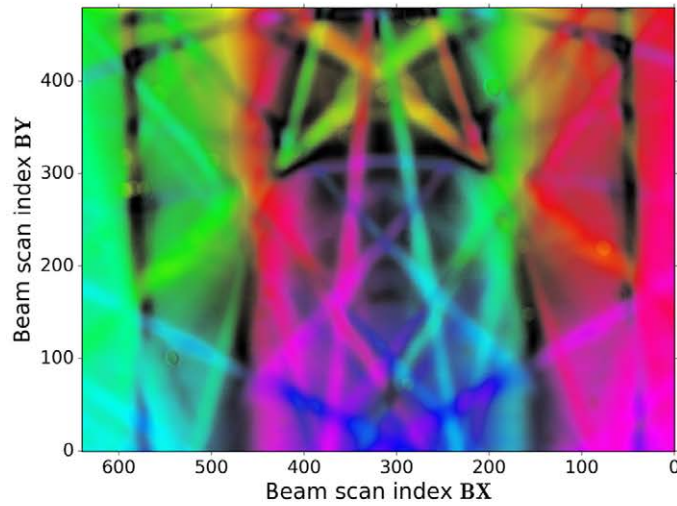
Quantification of the incident beam diffraction effects

So far, we have discussed the observed incident beam effects mainly qualitatively by referring to their symmetry. The determination of the projection centre of the measured EBSD patterns as discussed above makes it possible to actually quantify the incident beam diffraction effects on \mathbf{r}_{COM} by using the EBSD phosphor screen as a calibrated angular measurement device. We can thus calculate, e.g. the individual directions of \mathbf{r}_{COM} in the sample coordinate system for each pattern and analyse the angular deviation to the mean position $\bar{\mathbf{r}}_{\text{COM}}$ of all patterns. To this end, we show in Figure 8(A) the deviation angle from the mean of the unit vector corresponding to \mathbf{r}_{COM} in dependence of the measurement position for the data corrected for the electron beam movement. From Figure 8(A), we can estimate a maximum deviation effect of about 0.5° that can be assigned specifically to diffraction effects by reference to the clearly visible incident beam crystal geometry. We note that the deviation angle of \mathbf{r}_{COM} in our analysis is a proxy observable that is easily and reproducibly calculated directly from the measured 2D intensity array. Also, in a detailed, physics-based simulation of this intensity, the observable \mathbf{r}_{COM} would result in the same way from the theoretical models. A satisfactory physical model could thus obviously be judged by the level of the agreement of \mathbf{r}_{COM} with the experimental values and with other statistically descriptive properties of the observed data.

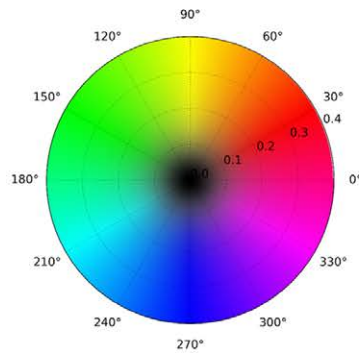
In addition to the absolute value of the deviation angle shown in Figure 8(A), we can use a colour key to represent both the polar and azimuthal angular deviation from the mean $\bar{\mathbf{r}}_{\text{COM}}$. The resulting map is shown in Figure 8(B) with the colour selected according to the colour key in Figure 8(C). Again, we can recognize the symmetry of the incident beam geometry in the complex colour changes that now quantify the angular changes of \mathbf{r}_{COM} near diffraction conditions.



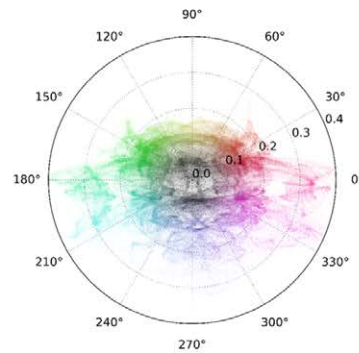
(A) Deviation angle of COM direction relative to mean COM direction



(B) Deviation of COM in polar coordinates



(C) Angular colour key



(D) COM vectors w.r.t. mean

Fig. 8. Quantification of incident beam effects on r_{COM} .

Figure 8(B) demonstrates how to practically apply statistical EBSD pattern properties such as \mathbf{r}_{COM} as an information channel for imaging. In particular, we can obtain *quantitative* information on the changes in \mathbf{r}_{COM} from the colour image shown in Figure 8(B). This is to be contrasted with the mainly *qualitative* colour information when using the ROI-based BSE image intensities as seen, for example in Figures 1, 3 and 6. Moreover, the assignment of a quantity like \mathbf{r}_{COM} to each map makes it also possible to display different aspects of the available information. For example, we can use a polar coordinate system to plot in Figure 8(D) the individual positions of \mathbf{r}_{COM} in each pattern relative to the mean $\bar{\mathbf{r}}_{\text{COM}}$. Similar to a common analysis tool in EBSD and general texture analysis, this could be seen as a ‘pole figure of \mathbf{r}_{COM} ’ which shows the information integrated over the spatial degrees of freedom. The range of practical usefulness of this kind of plot has yet to be tested, but one could imagine that such plots help to visualize specific correlations in high-dimensional data that would not be noticed otherwise. As an example, in Figure 8(D), we can distinguish correlations due to the symmetry of the incident beam *via* the characteristic, nearly mirror-symmetric concentrations of points. We realize that in Figure 8(D), the effects of the crystal symmetry related to the incident beam geometry have become apparent once again, albeit in a rather different way than as a function of the beam scan position.

Application to imaging

The measurements on the Si single crystal as discussed above were optimized in order to specifically single out the effects of incident beam diffraction (‘channelling-in’) on the backscattered electron angular intensity distribution. This was achieved by the analysis of symmetry effects in the COM position \mathbf{r}_{COM} .

As was already mentioned above, observables such as \mathbf{r}_{COM} and others can also provide an additional information source for EBSD-based imaging. In order to reveal the different information content of various data visualizations, we analysed a sample of a GaN thin film containing dislocations. This example is also relevant to the important topic of contrast interpretation in SEM-based dislocation imaging (Wilkinson & Hirsch, 1997; Picard *et al.*, 2012; Naresh-Kumar *et al.*, 2012; Picard *et al.*, 2014; Zaefferer & Elhami, 2014).

The data presented in this section were taken using a Merlin (Zeiss) FE-SEM at 20 kV and an e^- Flash^{HR+} EBSD detector (Bruker Nano). In Figure 9(A), we show a raw EBSP collected from the GaN sample. The characteristic influence of the collector position on the resulting images is demonstrated in Figures 9(B) and (C) which, respectively, show maps obtained by integrating the BSE signal from the top or bottom 10% of the respective pattern at each map position. Clearly, the dislocations are more directly visible in Figure 9(C) corresponding

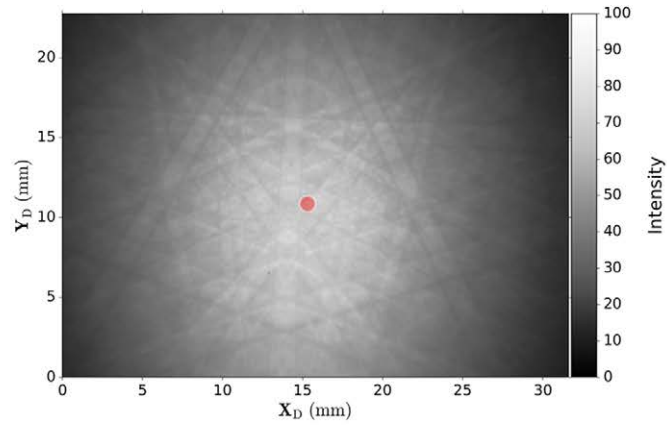
to the bottom 10% signal. In comparison, the sample topography with stepped structures is more clearly seen in Figure 9(B). Most importantly, there are contrast inversion effects between both images, including the regions influenced by dislocations. These observations emphasize that one needs to make sure that effects of the collector position are not influencing the interpretation of dislocation images.

The straightforward ‘virtual-BSE imaging’ shown in Figure 9 can be compared to images derived from an analysis of \mathbf{r}_{COM} for each individual pattern. As an example, the pertinent \mathbf{r}_{COM} is indicated by a red dot in Figure 9(A). With the determined \mathbf{r}_{COM} vectors providing a multidimensional signal, we can analyse their changes in selected spatial directions. To this end, in Figures 10(A) and (C), we show maps that correspond to the changes in the x and y pattern coordinates of \mathbf{r}_{COM} relative to the mean position $\bar{\mathbf{r}}_{\text{COM}}$. Note that we have used a different colour scheme compared to Figures 9(B) and (C) in order to emphasize that we are imaging conceptually different quantities in both cases: BSE intensity versus changes of a vector component, respectively. We can see that the x -change ΔCOM_X shown in the lower panel drastically emphasizes the contrast due to dislocations, whereas the upper panel with the y -change ΔCOM_Y is very similar to an inverted version of the lower panel of the previous Figure 9.

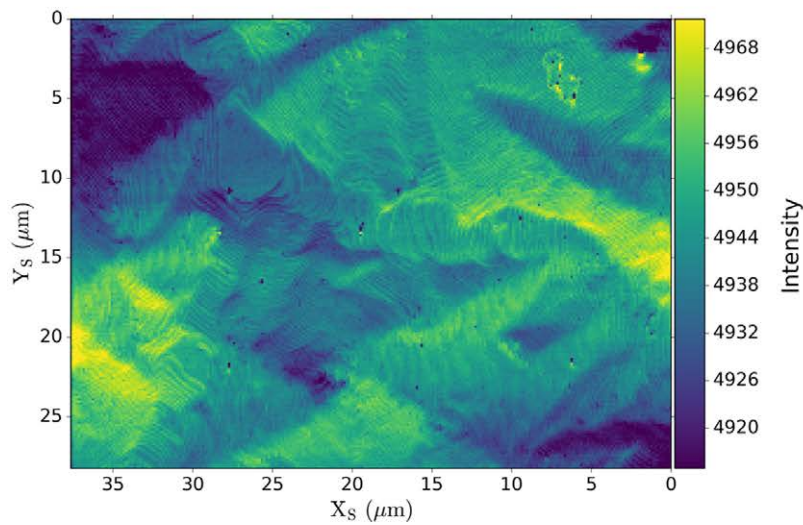
The specific choice of the information channel for EBSD imaging can also help to check the experimental data for parasitic external influences. Notably, the horizontal stripes which are seen in ΔCOM_X in Figure 10(C) are probably due to a periodic disturbance during the measurement. After noticing this effect in ΔCOM_X , we could confirm that this disturbance is already present in the raw data, although with much lower visibility.

Finally, the map data plotted in Figures 10(A) and (C) can be rearranged into a 2D histogram of the absolute positions of \mathbf{r}_{COM} in the measured patterns, which is shown in the middle panel (B) of Figure 10. This panel is using yet another different colour scheme to emphasize that we are now displaying the number of COM vectors that fall into a specific region of the detector. We can see from the histogram that the dominating number of patterns shows a change ΔCOM_X that is about half the variation of ΔCOM_Y in correspondence with the colour scale bars in the upper and lower panels, respectively. A larger topographic change in ΔCOM_Y than in ΔCOM_X can be expected due to the tilted sample geometry.

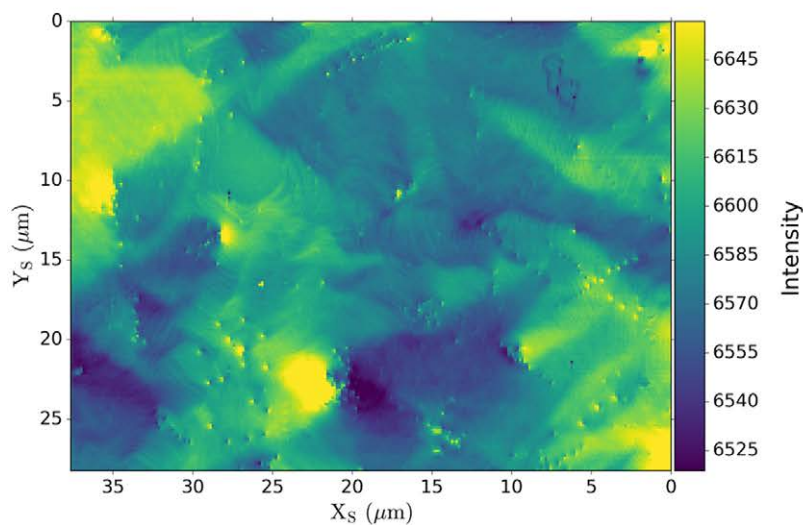
Summarizing our illustrative results for the GaN sample, we can distinguish the characteristic effects of the virtual collector position on the resulting BSE images and we can emphasize specific information such as effects caused by dislocations by visualizing ‘unconventional’ pattern properties like \mathbf{r}_{COM} . These observations imply that under the restricted detection conditions we have used, the contrast interpretation in SEM-based dislocation imaging can be influenced by the detection geometry.



(A) Raw EBSD pattern with r_{COM} marked by the red dot



(B) BSE signal from top 10% of patterns



(C) BSE signal from bottom 10% of patterns

Fig. 9. Virtual-BSE map from the GaN thin film sample for intensity taken from upper (B) or lower part (C) of the raw EBSD patterns (A). Topography is emphasized in (B), whereas dislocation features are emphasized in (C).

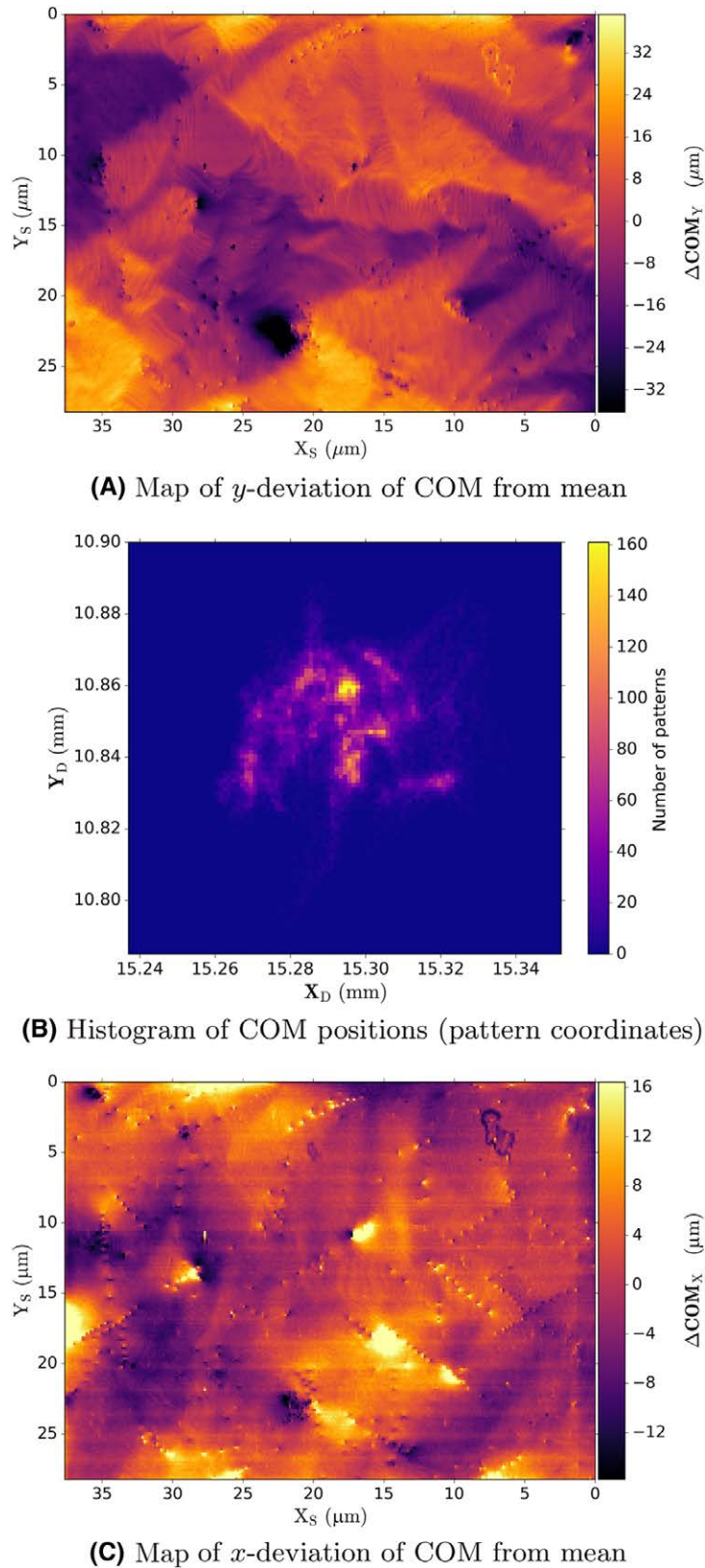


Fig. 10. Pattern-dependent centre of mass (\mathbf{r}_{COM}): Topography is visible in the map of the y -deviation (A) of \mathbf{r}_{COM} from the mean position $\bar{\mathbf{r}}_{\text{COM}}$ of all patterns in the map. The x -deviation of \mathbf{r}_{COM} in (C) emphasizes dislocation features as well as a periodic disturbance during the measurement that is seen as the horizontal stripes. (B): Histogram of the absolute \mathbf{r}_{COM} positions.

Conclusion

In accordance with the available literature of previous investigations, our observations have demonstrated the dominating influence of incident beam diffraction effects on the image formation process using angle-resolving BSE detectors. Complex orientation contrast features, which are visible in pseudocolour BSE images using multiple detectors, can be produced by changes of (1) the total BSE yield combined with (2) angular changes in this same total BSE yield under the influence of incident beam diffraction effects acting from the outset of the electron scattering cascade. In comparison to the large inelastic BSE signal, the backscattered Kikuchi pattern is usually such a small contribution that it cannot dominate the total image signal (Fig. 4).

The aim of this paper was to clearly prove the point (2): The so-called ‘channelling-in’ (incident beam diffraction) does not only change the total number of all backscattered electrons, but it also changes the directions in which these electrons are moving when they exit the sample. Near a diffraction condition, an electron detector with a limited acceptance angle can detect an increasing or decreasing number of electrons for different detector positions relative to the backscattered electron distribution. If multiple detectors are combined, complex colour changes can result which would not be explicable if all signals are simply scaled by a common, angle-independent factor proportional to the total or energy-resolved BSE yield.

We have applied the image property of the ‘centre of mass’ r_{COM} as a proxy observable that can clearly reveal the influence of the crystal symmetry in the incident beam geometry on the angular shape of the backscattered electron distribution. Moreover, r_{COM} also provides an additional information channel for EBSD-based topographic and orientation imaging in the SEM, which was demonstrated by the selective emphasis of dislocation features observed on a GaN thin film sample. It can be assumed that, in addition to the COM, other statistically descriptive properties of the BSE distribution, such as the standard deviation and other higher order moments, will deliver additional, more complete quantitative information which can be compared with physics-based simulations of the angle- and energy-dependent backscattering cross section from crystalline samples. In this way, the intricate intensity distributions in real-time pseudocolour SEM images like the one of the meteorite sample shown in Figure 1 will possibly be understood with quantitative crystallographic and topographic detail.

Acknowledgements

We would like to thank Philip Shields, University of Bath, Bath, U.K. for providing us with the GaN sample. The data presented in this paper is available on request from the corresponding author. This work was carried out with the support of EPSRC Grant Nos. EP/J015792/1 and EP/M015181/1 and through

support of a Carnegie Trust Research Incentive Grant No. 70483.

References

- Alam, M.N., Blackman, M. & Pashley, D.W. (1954) High-angle Kikuchi patterns. *Proc. R. Soc. A* **221**, 224–242.
- Böngeler, R., Golla, U., Kässens, M., Reimer, L., Schindler, B., Senkel, R. & Spranck, M. (1993) Electron-specimen interactions in low-voltage scanning electron microscopy. *Scanning* **15**, 1–18.
- Britton, T., Jiang, J., Guo, Y., Vilalta-Clemente, A., Wallis, D., Hansen, L., Winkelmann, A. & Wilkinson, A. (2016) Tutorial: crystal orientations and EBSD — or which way is up? *Mater. Charact.* **117**, 113–126.
- Buchwald, V.F. (1975) *Handbook of Iron Meteorites: Their History, Distribution, Composition, and Structure*. University of California Press, Berkeley, Los Angeles, London.
- Chapman, M., Callahan, P. & De Graef, M. (2016) Determination of sample surface topography using electron back-scatter diffraction patterns. *Scripta Materialia* **120**, 23–26.
- Curie, P. (1894) Sur la symétrie dans les phénomènes physiques. symétrie d'un champ électrique et d'un champ magnétique. *Journal de Physique* **3**, 393–415.
- Dapor, M. (2014) *Transport of Energetic Electrons in Solids*. Springer International Publishing, Cham, Switzerland.
- Day, A.P. (2009) *Spherical Kikuchi maps and other rarities. Electron Backscatter Diffraction in Materials Science* (ed. by A. J. Schwartz, M. Kumar, B. L. Adams & D. P. Field), pp. 65–80, 2nd edn. Springer Science + Business Media, New York.
- Day, A.P. & Quedsted, T.E. (1999) A comparison of grain imaging and measurement using horizontal orientation and colour orientation contrast imaging, electron backscatter pattern and optical methods. *J. Microsc.* **195**, 186–196.
- Dingley, D. (2004) Progressive steps in the development of electron backscatter diffraction and orientation imaging microscopy. *J. Microsc.* **213**, 214–224.
- Dudarev, S.L., Rez, P. & Whelan, M.J. (1995) Theory of electron backscattering from crystals. *Phys. Rev. B* **51**, 3397–3412.
- Forbes, B.D. & Allen, L.J. (2016) Modeling energy-loss spectra due to phonon excitation. *Phys. Rev. B* **94**, 014110.
- Goldstein, J.I., Newbury, D.E., Echlin, P., Joy, D.C., Lyman, C.E., Lifshin, E., Sawyer, L. & Michael, J.R. (2003) *Scanning Electron Microscopy and X-Ray Microanalysis*. Springer, Boston.
- Hejna, J. (1995) Topographic and material contrast in low-voltage scanning electron microscopy. *Scanning* **17**, 387–394.
- Hejna, J. (2008) Application of channel electron multipliers in an electron detector for low-voltage scanning electron microscopy. *J. Microsc.* **232**, 369–378.
- Hohn, F. & Niedrig, H. (1972) Elektronenrückstreuung an dünnen metall- und isolatorschichten. *Optik* **35**, 290–295.
- Hohn, F.J. (1977) Angular dependence of electron intensities backscattered from carbon films. *Optik* **47**, 491–494.
- Ichinokawa, T., Nishimura, M. & Wada, H. (1974) Contrast reversals of pseudo-Kikuchi band and lines due to detector position in scanning electron microscopy. *J. Phys. Soc. Jpn.* **36**, 221–226.
- Jackson, M.A., Groeber, M.A., Uchic, M.D., Rowenhorst, D.J. & Graef, M. (2014) h5ebds: an archival data format for electron back-scatter diffraction data sets. *Integr. Mater. Manuf. Innovat.* **3**, 4.

- Jähne, B. (2005) *Digital Image Processing*. 6th edn. Springer, Berlin Heidelberg.
- Jaksch, H. (2012) What BSE electrons can tell us. From ECCI via RBS to low loss BSE imaging. *Microsc. Microanal.* **18**, 680–681.
- Joy, D.C. (1995) *Monte Carlo Modeling for Electron Microscopy and Microanalysis*. Oxford University Press, New York, Oxford.
- Joy, D.C., Newbury, D.E. & Davidson, D.L. (1982) Electron channeling patterns in the scanning electron microscope. *J. Appl. Phys.* **53**, R81–R122.
- Naresh-Kumar, G., Hourahine, B., Edwards, P. *et al.* (2012) Rapid nondestructive analysis of threading dislocations in wurtzite materials using the scanning electron microscope. *Phys. Rev. Lett.* **108**, 135503.
- Niedrig, H. (1977) Film-thickness determination in electron microscopy: the electron backscattering method. *Optica Acta* **24**, 679–691.
- Niedrig, H. (1978) Physical background of electron backscattering. *Scanning* **1**, 17–34.
- Niedrig, H. (1982) Electron backscattering from thin films. *J. Appl. Phys.* **53**, R15–R49.
- Payton, E.J. & Nolze, G. (2013) The backscatter electron signal as an additional tool for phase segmentation in electron backscatter diffraction. *Microsc. Microanal.* **19**, 929–941.
- Peng, L.-M., Dudarev, S.L. & Whelan, M.J. (2004) *High-Energy Electron Diffraction and Microscopy*. Oxford University Press, Oxford, New York.
- Picard, Y.N., Kamaladasa, R., De Graef, M., Nuhfer, N.T., Mershon, W.J., Owens, T., Sedlacek, L. & Lopour, F. (2012) Future prospects for defect and strain analysis in the SEM via electron channeling. *Microsc. Today* **20**, 12–16.
- Picard, Y.N., Liu, K.X., Stahlbush, R.E., Twigg, M.E., Zhang, X. & Skowronski, M. (2008) Nondestructive dislocation delineation using topographically enhanced imaging of surface morphologies in 4H-SiC epitaxial layers. *J. Appl. Phys.* **103**, 074904.
- Picard, Y.N., Liu, M., Lammatao, J., Kamaladasa, R. & De Graef, M. (2014) Theory of dynamical electron channeling contrast images of near-surface crystal defects. *Ultramicroscopy* **146**, 71–78.
- Prior, D.J., Trimby, P.W., Weber, U.D. & Dingley, D.J. (1996) Orientation contrast imaging of microstructures in rocks using forescatter detectors in the scanning electron microscope. *Miner. Mag.* **60**, 859–869.
- Rau, E.I. & Reimer, L. (2001) Fundamental problems of imaging subsurface structures in the backscattered electron mode in scanning electron microscopy. *Scanning* **23**, 235–240.
- Reimer, L. (1998) *Scanning Electron Microscopy — Physics of Image Formation and Microanalysis*. 2nd edn. Springer Verlag, Berlin Heidelberg, New York.
- Reimer, L., Heilers, U. & Saliger, G. (1986) Kikuchi band contrast in diffraction patterns recorded by transmitted and backscattered electrons. *Scanning* **8**, 101–118.
- Schwartz, A.J., Kumar, M., Adams, B.L. & Field, D.P. eds. (2009) *Electron Backscatter Diffraction in Materials Science*. 2nd edn. Springer, Berlin.
- Schwarzer, R.A. & Sukkau, J. (2013) Electron back scattered diffraction: current state, prospects and comparison with x-ray diffraction texture measurement. *Banaras Metall.* **18**, 1–11.
- Shubnikov, A. & Koptsik, V. (1974) *Symmetry in Science and Art*. Plenum Press, New York.
- Spranck, M., Kässens, M. & Reimer, L. (1995) Influence of the angular distribution of backscattered electrons on signals at different take-off angles in low-voltage scanning electron microscopy (LVSEM). *Scanning* **17**, 97–105.
- Venables, J.A., Batchelor, D.R., Hanbücken, M., Harland, C.J. & Jones, G.W. (1986) Surface microscopy with scanned electron beams. *Philos. Trans. R. Soc. A* **318**, 243–257.
- Vos, M. & Winkelmann, A. (2016) Two-dimensional Kikuchi patterns of Si as measured using an electrostatic analyser. *Ultramicroscopy* **171**, 19–25.
- Walker, C.G., Frank, L. & Müllerova, I. (2016) Simulations and measurements in scanning electron microscopes at low electron energy. *Scanning* **38**, 802–818.
- Wells, O.C. (1974) *Scanning Electron Microscopy*. McGraw-Hill, New York.
- Wells, O.C. (1970) New contrast mechanism for scanning electron microscope. *Appl. Phys. Lett.* **16**, 151–153.
- Wells, O.C. (1979) Effects of collector take-off angle and energy filtering on the BSE image in the SEM. *Scanning* **2**, 199–216.
- Wells, O.C. (1999) Comparison of different models for the generation of electron backscattering patterns in the scanning electron microscope. *Scanning* **21**, 368–371.
- Wells, O.C., Gordon, M.S. & Gignac, L.M. (2012) Past, present, and future of backscatter electron (BSE) imaging. *Proc. SPIE* **8378**, 837802–837808.
- Werner, W.S.M. (2001) Electron transport in solids for quantitative surface analysis. *Surf. Interface Anal.* **31**, 141–176.
- Wilkinson, A.J. & Hirsch, P.B. (1997) Electron diffraction based techniques in scanning electron microscopy of bulk materials. *Micron* **28**, 279–308.
- Winkelmann, A., Trager-Cowan, C., Sweeney, F., Day, A.P. & Parbrook, P. (2007) Many-beam dynamical simulation of electron backscatter diffraction patterns. *Ultramicroscopy* **107**, 414–421.
- Wright, S.I. & Nowell, M.M. (2006) EBSD image quality mapping. *Microsc. Microanal.* **12**, 72–84.
- Wright, S.I., Nowell, M.M., de Kloe, R., Camus, P. & Rampton, T. (2015) Electron imaging with an EBSD detector. *Ultramicroscopy* **148**, 132–145.
- Yamamoto, T. (1977a) A note on the contrast mechanism of electron channeling patterns in scanning electron microscopy. *Phys. Status Solidi (A)* **43**, K53–K56.
- Yamamoto, T. (1977b) Experimental aspects of electron channeling patterns in scanning electron microscopy. I. Measurement of contrast. *Phys. Status Solidi (A)* **44**, 137–146.
- Yamamoto, T. (1977c) Experimental aspects of electron channeling patterns in scanning electron microscopy. II. Estimation of contrast depth. *Phys. Status Solidi (A)* **44**, 467–476.
- Yamamoto, T., Mori, M. & Ishida, Y. (1978) Contrast mechanisms in electron-channelling patterns and lattice-defect images obtained with a scanning electron microscope. *Philos. Mag. A* **38**, 439–461.
- Zaefferer, S. & Elhami, N.N. (2014) Theory and application of electron channelling contrast imaging under controlled diffraction conditions. *Acta Mater.* **75**, 20–50.

Supporting Information

Additional Supporting information may be found in the online version of this article at the publisher's website:

Figure S1: The centres of mass of 640×480 electron backscatter diffraction patterns as measured for each point of an electron channelling pattern from a silicon sample. Each position of the centre of mass is shown as a semitransparent disc.

Overlapping of discs is caused by deviations of the centre of mass from a regular scanning grid and these deviations then produce the darker areas, which have the symmetry of the incident beam geometry. The observation of this specific symmetry allows us to identify the incident beam diffraction ('channelling-in') as the cause of the diffraction-modulated changes in the centre of mass. Please note that the figure above directly displays the two-dimensional (X_D, Y_D) positions of all the centres of mass which were measured, which is to be compared to a one-dimensional *intensity* value on

predefined grid points of an electron channelling pattern. The reader is encouraged to zoom in on the figure to the maximum possible amount in order to see the local arrangement of the 30 7200 data discs, which all have the same grey value, i.e. no individual intensity is assigned to the two-dimensional data point in this case. As is discussed in the main text, both observables, the BSE intensity and the deviation of the centre of mass, show a similar symmetry, which must be due to a cause that has at most this symmetry, or less (Curie's principle).